1 ECOMAN: an open-source package for geodynamic and

2 seismological modeling of mechanical anisotropy.

3 Manuele Faccenda[1*], Brandon P. VanderBeek[1*], Albert de Montserrat[2], Jianfeng Yang[3], Neil Ribe[4]

4 [1]Dipartimento di Geoscienze, Università di Padova, 35131, Padova, Italy.
5 [2]Institute of Geophysics, ETH Zürich, Sonneggstrasse 5, 8092, Zürich, Switzerland.
6 [3]State Key Laboratory of Lithospheric Evolution, Institute of Geology and Geophysics, Chinese Academy of Sciences, Beijing,
7 China.
8 [4]Lab FAST, Univ Paris-Saclay, CNRS, Bat 530, rue André Rivière, F-91405 Orsay, France.
9

10 *Correspondence to*: Manuele Faccenda (manuele.faccenda@unipd.it), Brandon P. Vanderbeek
11 (brandonpaul.vanderbeek@unipd.it)

12 **Abstract.** Mechanical anisotropy related to rock fabrics is a proxy for constraining the Earth's deformation patterns. However,

13 the forward and inverse modelling of mechanical anisotropy in 3D large-scale domains has been traditionally hampered by the

14 intensive computational cost and the lack of a dedicated, open-source computational framework. Here we introduce ECOMAN,

15 a software package for modelling strain-/stress-induced rock fabrics and testing the effects of the resulting elastic and viscous

16 anisotropy on seismic imaging and mantle convection patterns.

17 Differently from existing analogous software, the modelling of strain-induced fabrics has been extended to all mantle levels

18 and it has been optimised to run across multiple CPUs, yielding strong scaling efficiency. In addition, shape preferred

19 orientation (SPO)-related structures can be modelled and superimposed over lattice/crystallographic preferred orientation

20 (LPO/CPO) fabrics, which allows the consideration of the mechanical effects of fluid-filled cracks, foliated/lineated grain-

21 scale fabrics and rock-scale layering.

22 One of the most important innovations is the Platform for Seismic Imaging (PSI), a set of programs for performing forward

23 and inverse seismic modelling in isotropic/anisotropic media using real or synthetic seismic datasets. The anisotropic inversion

24 strategy is capable of recovering parameters describing a tilted transversely isotropic (TTI) medium, which is required to

25 reconstruct 3D structures and mantle strain patterns and to validate geodynamic models.

26 1 Introduction

27 The study of the Earth's interior has been traditionally based on seismological and geodynamic modelling, the former providing

28 important information about its present-day structure, composition and state (Chang et al., 2015; French and Romanowicz,

29 2015; Schaeffer et al., 2016; Debayle et al., 2020), and the latter about its dynamics and compositional evolution (Davies et

30   al., 2012; Crameri and Tackley, 2014; Müller et al., 2022). Seismological and geodynamical modelling are very often
31   conducted independently, which creates mechanical and geometrical inconsistencies across the models, hampers the
32   interpretation of seismic observations in terms of geodynamic processes, and exacerbates the non-uniqueness of geodynamic
33   model predictions. An alternative approach is combining computational seismology and geodynamics with mineral physics,
34   which provides a comprehensive understanding of the Earth's interior processes, seismic behaviour, and material properties.
35   This multidisciplinary methodology has been used in previous studies to post-process geodynamic flow calculations with
36   thermodynamically self-consistent models of mantle mineralogy and converting thermal structure into isotropic elastic
37   parameters. The obtained seismic mantle structure can then be used in simulations of global wave propagation, such that
38   specific hypotheses on mantle dynamics can be tested directly against seismic data (Styles et al., 2011; Schubert et al., 2012;
39   Maguire et al., 2018). The inverse procedure consists in converting seismic anomalies into density anomalies driving mantle
40   flow models and is typically employed to quantify dynamic topography and mantle viscosity structure, and to reproduce large-
41   scale mantle flow patterns (e.g., Bunge et al., 2003; Steinberger and Calderwood, 2006; Rudolph et al., 2015). However,
42   isotropic seismic imaging provides limited information regarding local-/regional-scale dynamical processes (Fraters and
43   Billen, 2021), and a better way to couple the geodynamic evolution and seismological structure of the Earth's interior is by
44   accounting for the strain-/stress-induced mechanical anisotropy of crustal and mantle rocks.

45   Mechanical anisotropy refers to the directional dependence of mechanical properties in a material, and is well known to affect
46   both elastic and viscous deformational behaviour. Mechanical anisotropy depends on several factors, including the lattice or
47   crystal preferred orientation (LPO, CPO) of intrinsically anisotropic minerals, and extrinsic mechanisms related to the shape
48   preferential orientation (SPO) of melt, fluid, or air-filled fractures and non-spherical pores, and grain- or rock-scale
49   compositional layering. Most micro- and macro-scale fabrics are acquired as a function of the cumulative deformation and
50   material mechanical properties, and as such they constitute an important source of information about the Earth's dynamical
51   behaviour.

52   Elastic anisotropy is directly connected to seismic anisotropy, which is a phenomenon in which the seismic wave speed varies
53   as a function of the propagation direction. It is mainly observed in the crust, mantle boundary layers, and inner core (Almqvist
54   and Mainprice, 2017; Karato, 1998; Kendall, 2000; Long and Becker, 2010; Deuss, 2014). Understanding and modelling
55   seismic anisotropy is crucial for determining long-term deformational patterns and the present-day stress field in the crust, and
56   constraining geodynamic modelling predictions (Jadamec and Billen, 2010; Hu et al., 2017; Zhou et al., 2018; Lo Bue et al.,
57   2022). In addition, the ability to account for anisotropic effects can improve the quality of subsurface imaging. Indeed, it has
58   been demonstrated that, because of the uneven seismic ray coverage, failing to account for seismic anisotropy may generate
59   strong artefacts that substantially bias our understanding of mantle structures and dynamics in different tectonic settings
60   (Bezada et al., 2016; VanderBeek and Faccenda, 2021; VanderBeek et al., 2023; Faccenda and VanderBeek, 2023).
61   Considering the widespread presence of seismic anisotropy, anisotropic seismic models provide a more realistic representation
62   of the Earth's subsurface compared to isotropic models.

63 Viscous anisotropy modelling refers to the study and simulation of materials that exhibit varying degrees of viscosity
64 (resistance to viscous deformation) in different directions. Although viscous anisotropy has been traditionally associated with
65 the mechanical behaviour of multi-layered media (Mühlhaus et al., 2002; Kocher et al., 2006), it has been also observed in
66 experimentally-deformed mica-rich and olivine crystal aggregates (Shead and Kronenberg, 1993; Hansen et al., 2012).
67 Previous numerical studies demonstrated that viscous anisotropy can potentially stabilise long-wavelength convective patterns
68 (Christensen, 1987; Mühlhaus et al., 2004) and more generally affect processes such as plate motion (Kiraly et al., 2020), post-
69 glacial rebound (Han and Wahr, 1997), lithospheric shear zone reactivation (Tommasi et al., 2009) and dripping (Lev and
70 Hager, 2008).

71 Over the last few years a few attempts have been made to integrate micro-mechanical modelling of fabric evolution with large-
72 scale geodynamic models using either directors (Lev et al., 2008; Halter et al., 2022), the CPO model D-REX (Kaminski et
73 al., 2004; Becker et al., 2006; Jadamec and Billen, 2010; Faccenda and Capitanio, 2013; Faccenda, 2014; Ito et al., 2014; Hu
74 et al., 2017; Zhou et al., 2018; Fraters and Billen, 2021), or the CPO model Visco-Plastic Self Consistent (VPSC; Tommasi et
75 al., 2009; Li et al., 2014). However, each of these methodologies has its own limitations mainly associated with either the
76 accuracy of the estimates, the large computational burden or software accessibility, which have impeded a more widespread
77 diffusion in the geodynamic community. At the same time, the recovery of 3D seismic anisotropy patterns has been
78 traditionally considered intractable due to the highly underdetermined nature of the inverse problem, and only recently a
79 theoretical background and computational algorithms have been developed to invert for body wave seismic anisotropy in 3D
80 anisotropic media (VanderBeek and Faccenda, 2021; Rappisi et al., 2022; Wang and Zhao, 2022; VanderBeek et al., 2023;
81 Del Piccolo et al., 2023). Yet, to date there is no freely-available software capable of modelling seismic anisotropy related to
82 arbitrarily oriented structures.

83 In this contribution we present the new and open-source software package ECOMAN (**E**xploring the **CO**nsequences of
84 **M**echanical **AN**isotropy) that enables linking seismology and geodynamics by providing a set of computationally optimised
85 programs for (i) estimating rock mechanical anisotropy as a function of the geodynamic model deformation history, and
86 compositional, rheological, stress, pressure, temperature, fields, and (ii) solving forward/inverse seismological problems
87 accounting for seismic anisotropy. In the next sections, we first describe the different ECOMAN modules, after which we
88 discuss the advantages and limitations of the software package, and the roadmap for future developments.

89

90 Table 1. Abbreviations and their description. Units are indicated for dimensional physical properties.

Abbreviation	Description	
UM	Upper mantle	
UTZ	Upper mantle transition zone	

LTZ	Lower mantle transition zone	
LM	Lower mantle	
LPO/CPO	Lattice/crystal preferred orientation	
SPO	Shape preferred orientation	
FSE	Finite Strain Ellipsoid, defined by the eigenvalues and eigenvectors of **LS**	
STILWE	Smoothed Transversely Isotropic Long-Wavelength Equivalent	
DEM	Differential Effective Medium	
VPSC	Visco-Plastc Self Consistent	
MDM	Modified Director Method	
		Units
ρ	Density	kg/m^3
P	Pressure	Pa
T	Temperature	K
Fd	Fraction of dislocation creep deformation	-
V, V_i	Velocity vector and its components	m/s
F, F_{ij}	2nd-order deformation gradient tensor and its components	-
LS, LS_{ij}	2nd-order left stretch tensor and its components	-
C, $C_{\alpha\beta}$	4th-order elastic tensor and its components in Voigt notation	GPa
$\boldsymbol{\eta}$, $\eta_{\alpha\beta}$	4th-order normalised viscous tensor and its components in Voigt notation	-

91

2 Software package structure

93 ECOMAN includes several programs that are complementary and can be grouped into three main categories (Fig. 1):

94

1) programs that estimate strain/stress-induced rock fabrics (LPO and SPO) and their elastic and viscous anisotropic mechanical properties (D-REX_S, D-REX_M, EXEV);

2) programs that post-process the simulated rock fabrics for visualisation of their isotropic/anisotropic mechanical properties and deformational history (VIZTOMO, VIZVISC), and format the elastic tensors generating input files for seismological synthetics (VIZTOMO);

3) programs that test the elastic response of anisotropic media by performing seismological forward/inverse modelling and, in particular, isotropic and anisotropic seismic tomographies on synthetic and real seismic datasets (SKS-SPLIT, PSI).

Most of the code modules are written in the Fortran programming language, except for the PSI program that is written in Julia. Visualisation of the output is done through the MATLAB MTEX toolbox (Mainprice et al., 2011) for single aggregate fabrics, and ParaView (Ahrens et al., 2005) for 2D and 3D simulations.
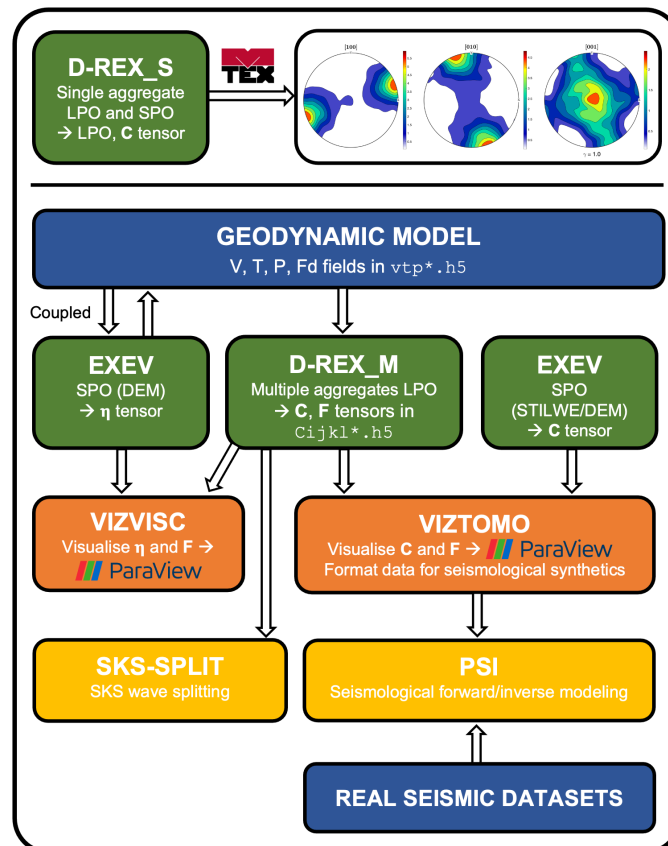

Figure 1. ECOMAN structure and flow chart. Coloured boxes denote programs that compute rock fabrics (green), post-process the elastic (**C**), viscous (**η**) and deformation gradient (**F**) tensors for visualisation and/or data formatting for seismological synthetics (orange), and perform seismological forward/inverse modelling on synthetic or real datasets (yellow). Input data are from geodynamic modelling or real

112 seismic datasets (blue). Visualisation of the mechanical properties and LPO can be done with the MTEX MATLAB toolbox for single crystal
113 aggregates or the software ParaView for large-scale simulations.

114

2.1 Rock fabrics and mechanical properties simulations

116 The evolution of the strain-induced LPO can be simulated for a single (D-REX_S) or multiple (D-REX_M) two-mineral phase

117 mantle aggregates. Five two-mineral phases mantle aggregates can be defined as a function of depth or density ρ (see Table 1

118 for a list of abbreviations and physical properties):

119

1) **olivine** + **enstatite**, for the upper mantle (UM: 0-410 km or $3000 < \rho \leq 3650$ kg/m^3);

2) **wadsleyite** + majoritic garnet, for the upper mantle transition zone (UTZ: 410-520 km or $3650 < \rho \leq 3870$ kg/m^3);

3) ringwoodite + majoritic garnet, for the lower mantle transition zone (LTZ: 520-660 km or $3870 < \rho \leq 4150$ kg/m^3);

4) **bridgmanite** + ferropericlase, for the lower mantle (LM: 660-2900 km or $\rho > 4150$ kg/m^3);

5) **post-perovskite** + ferropericlase, for the bottom of the lower mantle according to the phase boundary from Oganov and Ono (2004).

126

127 The strain-induced LPO is computed for the phases in bold, while other major phases such as garnet, ringwoodite and

128 ferropericlase are considered to be isotropic and their distribution is set to be random. Thus, no LPO is computed for the LTZ,

129 such that (minor) anisotropy arises only when SPO modelling due to compositional layering is active (section 2.1.3; Faccenda

130 et al., 2019). The full elastic tensor is then calculated according to the crystal orientation, volume fraction, phase abundance,

131 P-T conditions, bulk rock composition, and using Voigt-Reuss-Hill averaging schemes (see section 2.1.2 for more details).

132 The elastic properties related to strain/stress-induced SPO fabrics can instead be calculated at the grain- or rock-scale and for

133 layered or two-phase (matrix-ellipsoidal inclusions) systems using the isotropic elastic moduli of the different (fluid, mineral,

134 rock) components (EXEV).

135 The elastic properties and density of the aggregates characterised by LPO and/or SPO fabrics are estimated at relevant mantle

136 P-T conditions using the single crystal elastic moduli and their P-T derivatives for the main mineral phases and compiled from

137 different mineral physics studies, together with lookup tables of the isotropic elastic moduli, density and mineral phase volume

138 fraction generated with MMA_EoS (Chust et al., 2017) for five bulk rock compositions (dunite, harzburgite, pyrolite, MORB,

139 pyroxenite) and in the T = 300 : 50 : 4500 K, P = 0 : 0.1 : 140 GPa range.

2.1.1 D-REX_S

141 D-REX_S is a program designed for modelling the evolution of strain-induced LPO fabrics and related elastic properties of a

142 single, two-mineral phases mantle aggregate, as a function of the imposed flow field, amount of strain, crystal plasticity, P-T

143 conditions and additional effects related to SPO fabrics. It builds on the original D-REX software (Kaminski et al., 2004) for

144 modelling the strain-induced LPO, and it includes MATLAB scripts to generate pole figures of the LPO and

145 isotropic/anisotropic seismic properties with the MTEX software (Mainprice et al., 2011) (Fig. 2a-d), together with the

146 possibility to display the evolving fabric strength (M-index, J-index) and the fraction of different anisotropy components

147 (obtained via tensor decomposition; Browaeys et al., 2004; Fig. 2e-h).

148 D-REX_S is particularly useful for those users who are not familiar with LPO modelling, and more in general, to anyone

149 interested in performing parameter sensitivity tests on different mantle mineral aggregates before launching large-scale

150 simulations. In addition, the microstructures generated with D-REX_S can be used in the D-REX_M 2D-3D simulations to

151 impose pre-existing (e.g., fossil) fabrics on multiple crystal aggregates located within a specific subdomain (see section 2.1.2).

152

153
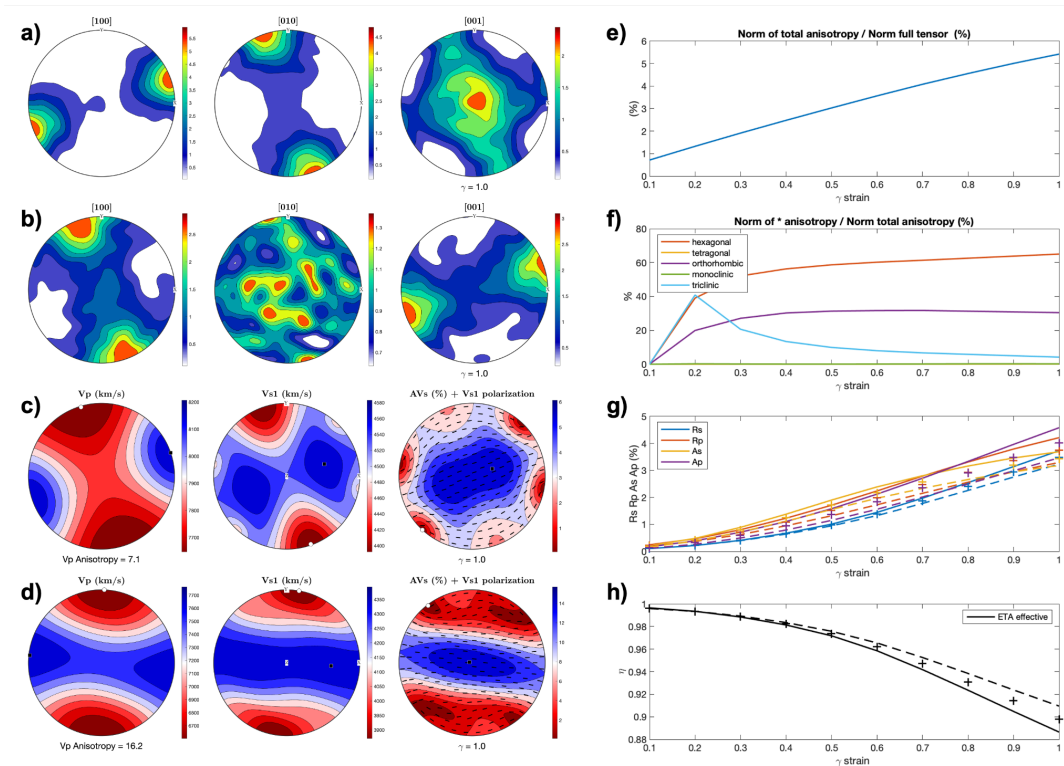
Figure 2. D-REX_S output for an upper mantle aggregate (Ol:Opx=70:30) subjected to a simple shear deformation of 1. Pole figures of the olivine (a) and orthopyroxene (b) crystallographic axes; (c) pole figures of Vp, Vs1, AVs = 200(Vs1 - Vs2)/(Vs1 + Vs2) with superimposed Vs1 polarisation directions evaluated from the elastic tensor of the two phase aggregate. (d) same as (c) but with the superimposed effect of an SPO fabric due to 5% melt-filled cracks aligned at -30° from the principal stress (i.e., at 15° from the horizontal plane); (e) fraction of total anisotropy relative to the full elastic tensor and (f) contribution of 5 anisotropic classes relative to the total anisotropy; (g) P- and S-wave radial and azimuthal anisotropy and (h) eta parameter = F/(A-2L) for the elastic tensors computed with the Voigt (continuous lines), Reuss (dashed lines) and Hill (crosses) averaging schemes, respectively.

161

162 **2.1.2 D-REX_M**

163 D-REX_M is a program that computes the evolution of the LPO and related elastic properties of multiple, two-mineral phases

164 mantle aggregates, as a function of the single crystal plastic and elastic properties, and of the flow field, deformation

165 mechanisms and P-T conditions resulting from 2D-3D geodynamic simulations. It builds on the original D-REX software,

166 which estimates the strain-induced LPO and elastic properties (i) for upper mantle polycrystalline aggregates only, (ii) using

167 single crystal elastic tensors derived at room P-T conditions and averaged using a Voigt scheme, (iii) in a 2D cartesian domain,

168 (iv) assuming steady-state flow, and (v) whereby the whole deformation is considered to be accommodated by dislocation

169 creep assisted by grain-boundary sliding (Kaminski et al., 2004). D-REX_M additionally models:

- 170 fabrics relevant to the mid and lowermost mantle (Faccenda, 2014), including those with post-perovskite. Phase
171 transitions can be set to occur at predefined depths (e.g., 410 km, 660 km). Density crossovers (which allow modelling
172 the deflection of phase boundaries with a non-null Clapeyron-slope; Fig. 5), and parameterized phase boundaries as
173 for the case of post-perovskite (Oganov and Ono, 2004) are also included;

- 174 elastic properties and density as a function of the bulk rock composition and local P-T conditions (Faccenda, 2014,
175 Chang et al., 2016, Ferreira et al., 2019). The isotropic component of the elastic tensors and density are taken from
176 the lookup tables generated by MMA-EoS for a given mantle lithology, and the anisotropic component from the
177 mineral single crystal elastic moduli and their pressure and temperature derivatives. This strategy ensures a gradual
178 transition of the seismic properties at phase boundaries where phase transformations occur. Voigt-Reuss-Hill
179 averaging schemes of the elastic moduli are included;

- 180 non steady-state flows in 2D/3D cartesian and polar grids (Faccenda and Capitanio, 2012, 2013, Hu et al., 2017; Zhou
181 et al., 2018; Lo Bue et al., 2022; Faccenda and VanderBeek, 2023). The global-scale models are spatially discretized
182 using the so-called Yin-Yang grids (Kageyama and Sato, 2004). Several examples (cookbooks) are provided on how
183 to use the software in different coordinate systems and in steady-state or time-dependent flow conditions;

- 184 fabric evolution in the presence of multiple creep mechanisms. At any time step, the fraction of deformation
185 accommodated by dislocation creep in a given point of the geodynamic model defines the fraction of time spent for
186 intracrystalline deformation assisted by grain-boundary sliding. The remaining time is used to apply, when present,
187 fluid deformation rotation to the whole crystal aggregate (e.g., Hedjazian et al., 2017);

- 188 a pre-existing (fossil) fabric (pre-computed with D-REX_S) within a subdomain, typically the lithosphere. This is
189 often the case for geodynamic models where the lithosphere accretion is not modelled, and its geometry is initially
190 prescribed;

191

192 The D-REX_M input files should contain information about the geodynamic model evolution. Critical information are the

193 components of the velocity vector **V** field, and, for time-dependent flow models, the total elapsed time and timestep. These are

194   used to compute the velocity gradient tensor, and the LPO evolution and advection of the crystal aggregates. Additional fields

195   defined on the cartesian/spherical grid that can be included in the input files are:

196   ● when the geodynamic model is thermo-mechanical, the temperature T and total pressure P fields, which can be used

197   to compute the single crystal elastic tensor and aggregate phase transitions as a function of the local P-T conditions;

198   ● when the rheological model of the geodynamic simulation is based on multiple visco-plastic deformation

199   mechanisms, the fraction of deformation accommodated by dislocation creep $Fd = \eta_{disl}/\eta_{eff}$, `where 0 ≤ Fd ≤ 1,`

200   η_{disl} is the viscosity calculated with the dislocation creep flow law, η_{eff} is the effective viscosity calculated with the

201   harmonic average of each of the viscosities representing a different deformation mechanism.

202

203   Summarising, the time and the velocity field **V** are essential information, while the P, T, Fd fields are optional and depend on

204   the type of (mechanical vs. thermomechanical) geodynamic and (single vs. multiple visco-plastic deformation mechanisms)

205   rheological models.

206   While the **V,** P, T, Fd fields are defined on the Eulerian grid, the distribution, size, modal composition and mechanical

207   properties of mantle aggregates are defined on the Lagrangian particles. After initialising the Eulerian grid and Lagrangian

208   particles, the entire run consists of three main steps: (i) backward advection of the particles; (ii) forward advection and update

209   of the LPO and deformation gradient tensor **F**; (iii) computation of the full elastic tensor and creation of the output file. The D-

210   REX_M output file(s) includes, for each mineral aggregate, the elastic tensor **C**, density, and the deformation gradient tensor

211   **F**. These properties can be then processed and visualised with the software VIZTOMO (section 2.2.1).

212   D-REX_M is parallelized using a hybrid MPI and OpenMP scheme to take advantage of multiple CPUs architectures of

213   modern HPC clusters. Runtime is obviously affected by the number of crystal aggregates, number of crystals per aggregate

214   and of active slip systems per crystal, and number of timesteps (Fig. 3, top). The parallel efficiency ranges 70-90%, and the

215   update of the LPO and **F** tensor during forward advection is the most time-consuming part of the run (Fig. 3, centre, bottom).

216   The small performance degradation is due to the initialization of the Eulerian/Lagrangian grids and arrays, and to I/O operations

217   which are executed serially within each process. As a result, the efficiency of the time-dependent flow models is lower than

218   that of steady-state models, as the latter only require a single velocity (and P, T, Fd) field to be loaded and processed.
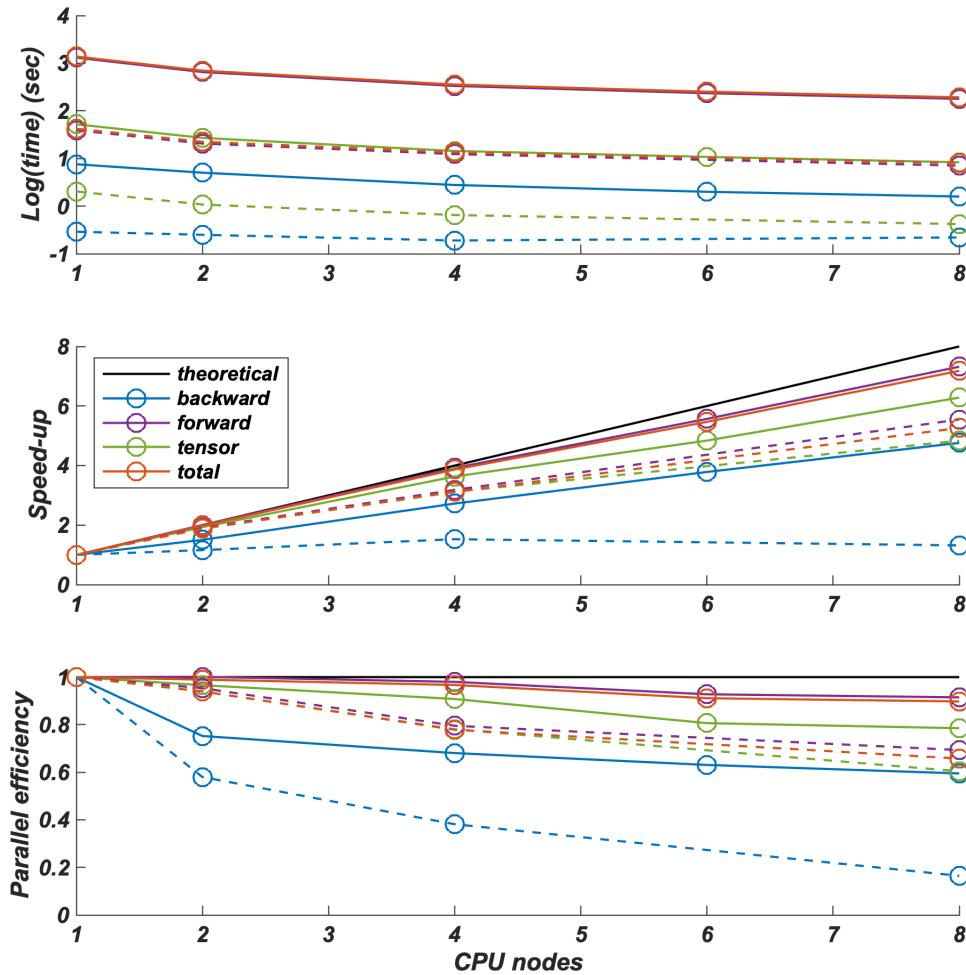
Figure 3. Runtime (top), speedup (centre) and parallel efficiency (bottom) of D-REX_M for initial backward advection of aggregates ("backward"), forward advection and updating of the LPO and **F** tensor ("forward"), full elastic tensor computation and output file creation ("tensor"), and entire run ("total"). Results are shown for two models included in the cookbooks: the 3Dspherical_global model (steady-state flow, 96 timesteps, 1327606 aggregates, LPO computed only for 260474 upper mantle aggregates) and the 3Dspherical_sinkingslab model (dashed lines; time-dependent flow, 20 timesteps, 38509 aggregates, LPO computed for 25177 upper mantle and 6587 upper mantle transition zone aggregates). Runs performed on a HPE Superdome Flex (8 CPUs, 28 cores Intel Xeon(R) PLATINUM 8180 @ 2.50GHz) using from 1 to 8 nodes.

2.1.3 EXEV

EXEV includes routines to compute the EXtrinsic Elastic and Viscous anisotropy using Effective Medium Theory modelling for a multi-component layered system (Smoothed Transversely Isotropic Long-Wavelength Equivalent, STILWE; Backus, 1962) or a two-component system with similar ellipsoidal inclusions in a uniform background matrix (Differential Effective Medium, DEM; e.g., Mainprice, 1997).

10

234 The elastic tensor **C** due to SPO fabrics can be either estimated independently or, when using the DEM approach, superimposed

235 on that obtained from the strain-induced LPO modelling. SPO fabrics that can be modelled are those related to rock- or grain-

236 scale layering (e.g., Faccenda et al., 2019), or to the presence of preferentially aligned ellipsoidal inclusions (e.g., melt-/fluid-

237 filled cracks). The user then needs to specify:

- for grain-scale layered fabrics, a dominant ultramafic or mafic lithology. In this case the mineral phase proportions from the MMa-EoS lookup tables define the mixture for the STILWE model;

- for rock-scale layered fabrics, the relative abundance of the five available ultramafic-mafic lithologies (dunite, harzburgite, pyrolite, basalt and pyroxenite) defining the mixture for the STILWE model;

- for matrix-inclusion fabrics, the elastic tensors of the two components and the inclusion's shape and volume fraction as required by the DEM modelling. The matrix elastic tensor can be replaced with that from the LPO modelling in order to estimate the combined effect of LPO and SPO fabrics.

245 The SPO fabrics can then be oriented at any angle relative to the principal Finite Strain Ellipsoid (FSE) axis or, in case of

246 cracks, the local principal stress obtained from the "present-day" (i.e., last) velocity field.

247 Summarising, SPO fabric modelling requires one or more of the following: **F** and/or **C** obtained from D-REX_M; P, T and/or

248 **V** and/or fluid/melt fraction fields for the "present-day" state of the geodynamic model. Consequently, this modelling is

249 performed when post-processing the D-REX_M output with the software VIZTOMO (see section 2.2.1).

250 The total or deviatoric component of the viscous tensor $\boldsymbol{\eta}$ due to SPO fabrics is estimated for two-phase systems with ellipsoidal

251 weak/hard inclusions using the DEM theory, and the parametrization of the viscous tensor evolution and orientation as a

252 function of the cumulated deformation (**F**) obtained following de Montserrat et al. (2022). Indeed, most if not all, mantle levels

253 are composed of two main mineral phases that control both the elastic and viscous properties. The case of a multi-component

254 layered medium is not considered because its viscous tensor can be either approximated with flat inclusions, or more simply

255 computed using the Voigt and Reuss averages of the layers' isotropic viscosity.

256 The first modelling phase requires running subprogram DEMviscous to generate a database of viscous tensors for a range of

257 inclusion shapes and volume fractions, and inclusion-matrix viscosity contrasts. The latter implies that the viscous moduli are

258 dimensionless and can therefore be interpreted as scaling factors with respect to an isotropic effective viscosity of the bulk

259 rock or most abundant mineral phase. Subsequently, the database can be exploited by large-scale geodynamic simulations to

260 either (i) return the viscosity tensor $\boldsymbol{\eta}$ from a look-up table for every point of the computational domain, which can be

261 superimposed on the isotropic effective viscosity computed from flow laws (coupled mechanical simulations), or (ii) estimate

262 $\boldsymbol{\eta}$ (uncoupled mechanical simulation) and/or visualise its anisotropic viscous properties for the "present-day" state of the

263 geodynamic model with the software VIZVISC (section 2.2.2).

264

2.2 Visualisation of the mechanical properties and data formatting in preparation for seismological synthetics

2.2.1 VIZTOMO

VIZTOMO processes the D-REX_M output for the visualisation of the aggregates' elastic and deformational history properties. Estimation of extrinsic anisotropy effects via the EXEV routines is possible at this stage. The properties of the **C** and **F** tensors can be determined either at the position of the Lagrangian mantle aggregates, or, in case of the elastic properties and density, interpolated to a structured (tomographic) grid. In the latter case the grid can be saved in a format suitable for generating synthetic seismic datasets via the PSI_D package (see section 2.3.2) or for 3D waveform simulations in SPECFEM (Komatitsch and Tromp, 1999).

Several properties of the elastic tensor **C** can be visualised:

- Isotropic or ray-path dependent velocity anomalies and anisotropic elastic properties of body-waves (i.e., P-wave anisotropy and direction of maximum P-wave velocity; direction and magnitude of maximum S-wave splitting delay time; S-wave radial and azimuthal anisotropy);
- reflection/transmission energies resulting from the whole range of P-S conversions occurring at discontinuities (useful for studies based on receiver function analysis);
- the fraction of the elastic tensor anisotropic component relative to the total and the relative contributions of five different anisotropy classes (hexagonal, orthorhombic, tetragonal, monoclinic, triclinic) obtained through elastic tensor decomposition (Browaeys et al., 2004);
- the orientation of the hexagonal symmetry axis (already present in the original D-REX).

The deformation history stored in **F** can be visualised in terms of the FSE shape and orientation and/or length or orientation of its minimum and maximum semi axes.

The different fields are saved in specific file formats which can be imported by the open source ParaView software (Ahrens et al., 2005) for visualisation. Figures 4, 5, 6, 7 display some of these fields computed for different geodynamic models.
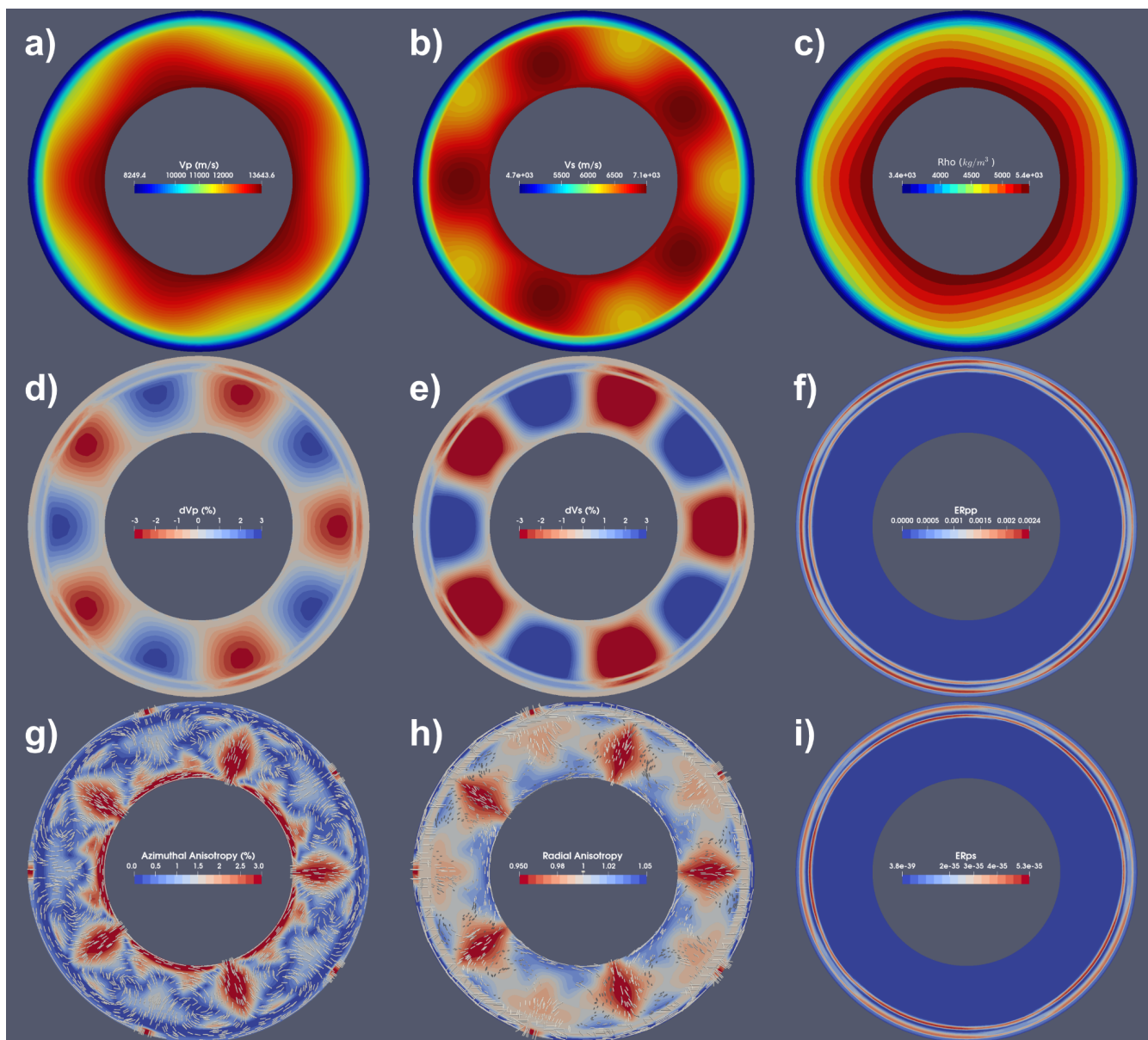
Figure 4. VIZTOMO output for the model 2Dpolar_convection available in the cookbooks. (a,b) isotropic Vp and Vs (m/s); (c) density; (d,e) isotropic P- and S-wave anomalies; (g) azimuthal anisotropy and FSE semi-axis (white bars); (h) radial anisotropy and TTI axis (white bars); (f,i) P-P and P-S reflection energy for waves propagating upward.
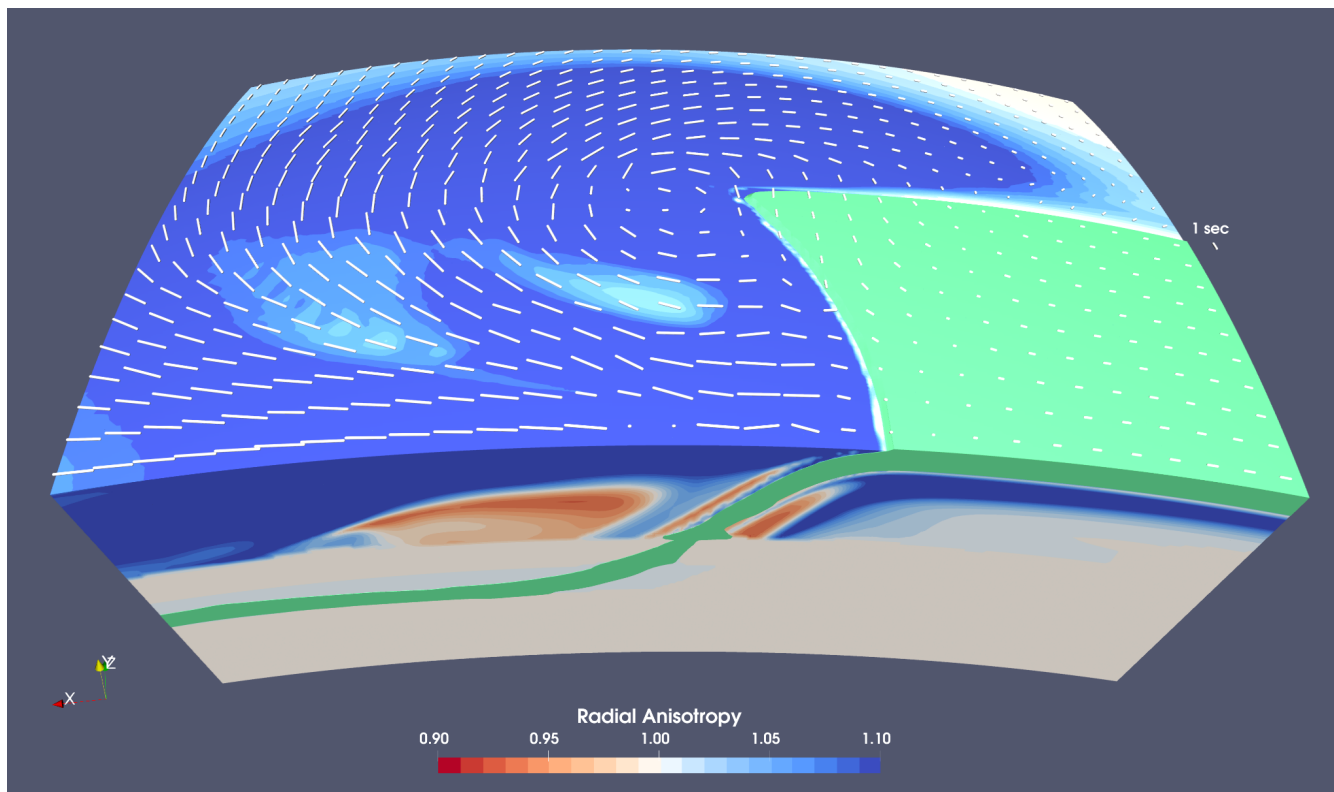
**Figure 5.** VIZTOMO output for a 3D model of oceanic plate subduction and roll back in spherical coordinates. Fabrics computed with D-REX_M for only upper mantle aggregates. A fossil A-type olivine fabric with the fast axis parallel to plate motion and computed with D-REX_S is initially defined within the oceanic plate volume. The colour scale indicates radial anisotropy in the upper mantle, and the white bars the SKS splitting computed with SKS-SPLIT. The volume in green encloses material with a +2% P-wave anomaly (i.e., the oceanic plate). Note the apparently thicker slab portion around the 410 km depth discontinuity, due to the upwelling of the olivine-spinel phase transition. The model domain extends from 0-1000 km along the radial direction, 85°-115° along longitude, and 70-90° along colatitude.
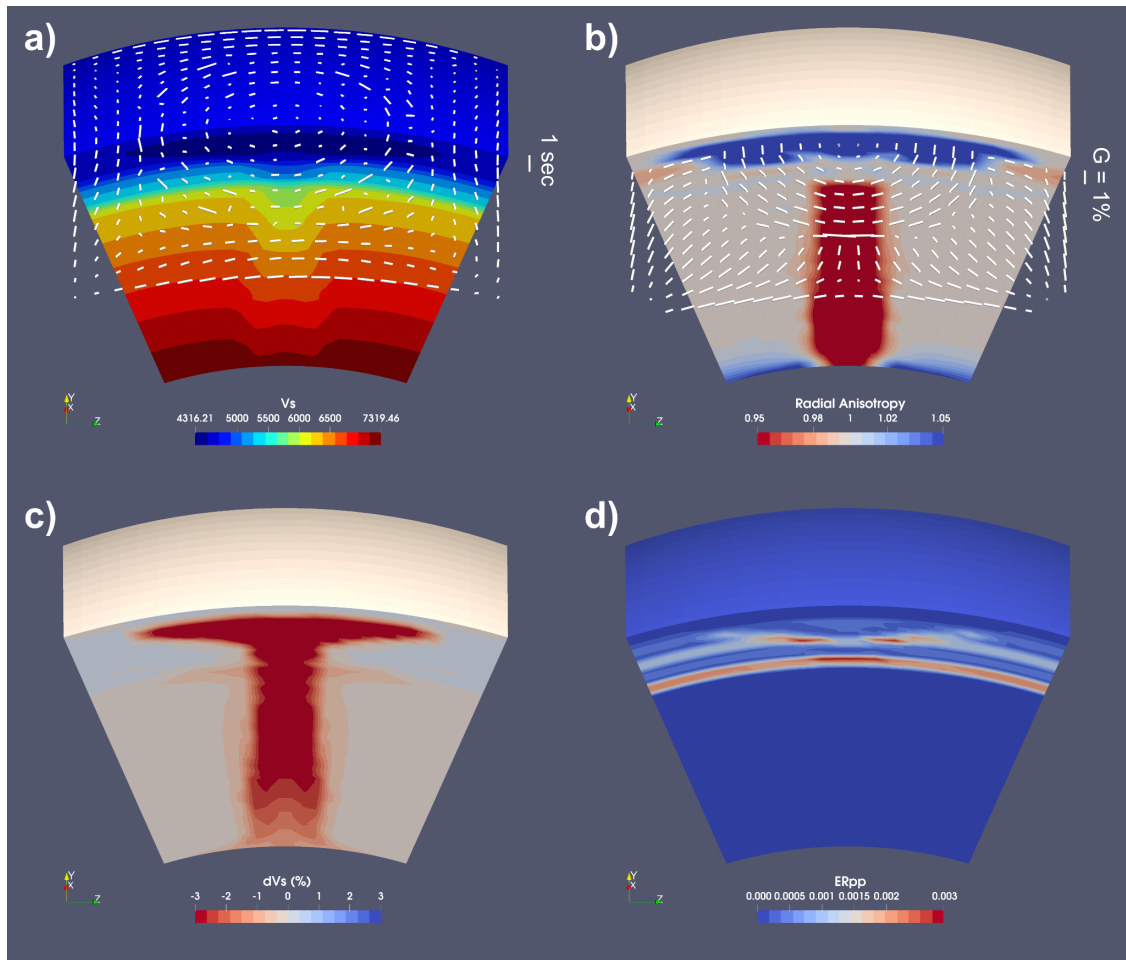
**Figure 6.** VIZTOMO output for an upwelling plume toy model in spherical coordinates. a) absolute Vs (m/s) and SKS splitting computed with SKS-SPLIT (white bars); b) radial anisotropy (colour scale) and azimuthal anisotropy at 200 km depth (white bars); c) isotropic Vs anomaly; d) P-P reflection energy for a wave propagating upward. The model domain extends from 0-2900 km along the radial direction, 70°-110° along longitude, and 70-110° along colatitude.
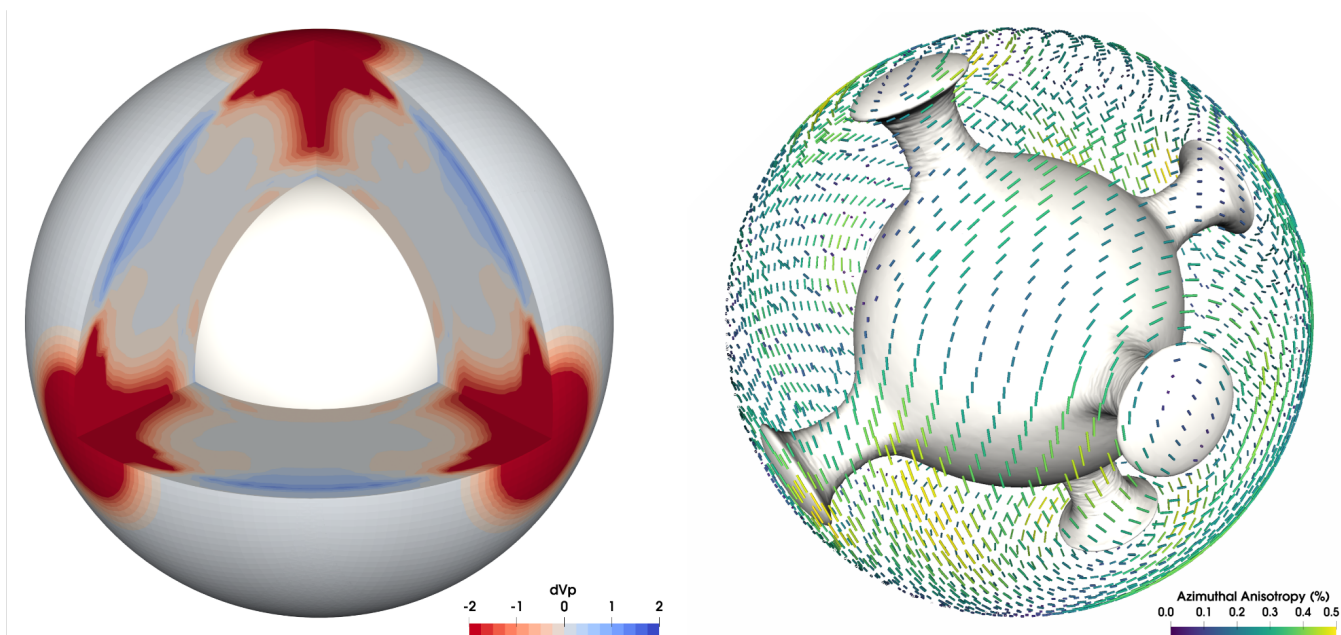
Figure 7: VIZTOMO output for the model 3Dspherical_global available in the cookbooks. Isotropic P-wave anomaly (left) and azimuthal anisotropy at 200 km depth (right). The grey surface encloses material hotter than the surrounding.

2.2.1 VIZVISC

VIZVISC processes the D-REX_M output for the visualisation of the aggregate properties such as the viscous anisotropy and related deformational history (in terms of the FSE) in ParaView. The deviation from isotropy is evaluated by computing the radial and azimuthal components of viscous anisotropy in a similar way as for the elastic tensor. More in detail, radial viscous anisotropy is defined as $\xi = N/L$, while azimuthal viscous anisotropy is defined by the magnitude $G = \sqrt{Gc^2 + Gs^2}$ and azimuth $\phi = tan^{-1}(Gs, Gc)$, where $N = \frac{1}{8}(\eta_{11} + \eta_{22}) - \frac{1}{4}\eta_{12} + \frac{1}{2}\eta_{66}$, $L = \frac{1}{2}(\eta_{44} + \eta_{55})$, $Gc = \frac{1}{2}(\eta_{55} - \eta_{44})$, $Gs = \eta_{45}$. Radial and azimuthal viscous anisotropy are evaluated in the FSE (and thus inclusions) reference frame, whereby the minor semi axis is oriented along the vertical direction, `and the intermediate and major semi axes are in the horizontal plane. As such, radial anisotropy is always ≥ 1.` Figure 8 displays some of these fields computed for a 2D steady-state model of mantle convection with periodic upwellings and downwellings.

16
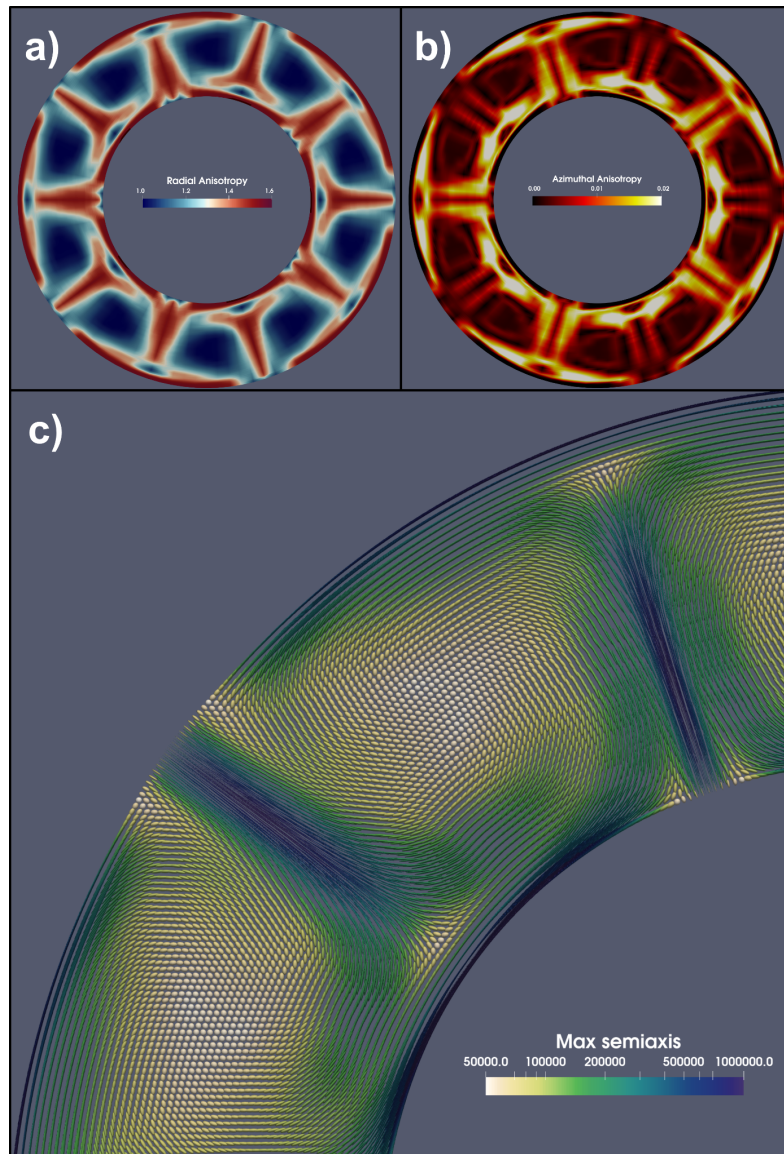
Figure 8. VIZVISC output for the model 2Dpolar_convection available in the cookbooks. (a) Radial viscous anisotropy; (b) azimuthal viscous anisotropy; (c) FSE shape coloured by the length of its major semi-axis upscaled by a factor of 50 km.

2.3 Seismic forward and inverse modelling

2.3.1 SKS-SPLIT

SKS-SPLIT estimates the SKS splitting at a grid of virtual seismic stations placed at the top of the D-REX_M model as a function of the back-azimuth using the Fortran routines included in FSTRACK (Schulte-Pelkum and Blackmann, 2003; Becker

17

329   et al., 2006). The routines have been adapted to load the D-REX_M output, stack the elastic tensors and densities in an upper

330   mantle rock column beneath each virtual seismic station (Faccenda and Capitanio, 2013), and run in parallel using MPI. The

331   averaged fast azimuth scaled by the delay time can then be visualised in ParaView as shown in Figures 5 and 6a.

332   **2.3.2 PSI**

333   PSI (Platform for Seismic Imaging) is a Julia package for performing tomographic inversion of both real and synthetic seismic

334   datasets. In the context of the ECOMAN software, it's a useful tool for exploring how features in high-resolution geodynamic

335   simulations are mapped into lower resolution seismic tomography models; this is a critical step if one aims to evaluate

336   geodynamic results against existing tomographic images.

337   PSI can be used to forward model P and S travel-times, splitting intensity (Chevrot, 2000), and shear wave splitting parameters

338   (i.e. the fast-polarisation azimuth and the delay time between the fast- and slow-polarised waveforms). Forward modelling of

339   these seismic observables is supported for three different model parameterizations: (1) isotropic P- and S-wavespeeds, (2)

340   hexagonally anisotropic media defined by the 5 Thomsen parameters and the azimuth and elevation of the symmetry axis, and

341   (3) fully anisotropic models defined by the density-normalised 21-component elastic tensor which can be generated from D-

342   REX_M + VIZTOMO (sections 2.1.2 and 2.2.1). Seismic phase velocities are computed following Thomsen (1986) for

343   hexagonally anisotropic models while the Christoffel equations are solved when the elastic tensor parameterization is used.

344   Anisotropic travel-times and splitting intensities for arbitrarily polarised S-waves are computed following VanderBeek et al.

345   (2023) using a long-wavelength approximation in which the accumulated delay time between fast- and slow-polarised qS-

346   waves is less than their dominant period. Lastly, splitting parameters are predicted using the matrix propagation method of

347   Rumpker and Silver (1998). In this initial release of PSI, all predictions are made via integration along ray paths traced through

348   a user-defined 1D reference velocity model using the TauP Toolkit (Crotwell et al. 1998). The 3D model properties are

349   subsequently interpolated to these paths before computing the seismic observables. We anticipate releasing an update to the

350   package that includes both 3D anisotropic ray tracing and finite-frequency kernels that are currently under development.

351   Travel-time and splitting intensity datasets can be inverted individually and jointly either for isotropic (Vp and Vs) or

352   hexagonally anisotropic model parameters. Hexagonal anisotropy is defined by up to five free parameters, the isotropic (1) P-

353   and (2) S-velocity, (3) anisotropic magnitude, and the (4) azimuth and (5) elevation of the hexagonal symmetry axis. Only a

354   single anisotropic magnitude parameter is required because the strength of P and S anisotropy is strongly correlated (e.g.,

355   Becker et al., 2006). Consequently, the ratios between the three Thomsen parameters ($\boldsymbol{\varepsilon}$, $\boldsymbol{\delta}$, $\boldsymbol{\gamma}$; Thomsen 1986) and the inverted

356   anisotropic magnitude parameter must be chosen *a priori* and can be spatially variable. Source and receiver statics for each

357   observation and seismic phase type may also be included as free parameters. The tomographic model is obtained by iteratively

358   solving a system of linearized equations relating the perturbations in the inversion parameters to the data residuals augmented

359   with damping and smoothing constraints. The solution is obtained via the LSQR algorithm (Paige & Saunders, 1982). Full

360   details on the tomographic method can be found in VanderBeek and Faccenda (2021) and VanderBeek et al. (2023). The final

361   tomographic solution is written to a VTK file to be visualised in ParaView. Tomographic inversions can be run from a

362   workstation. For problems consisting of ~1e4 observations and ~1e5 parameters, solutions can be obtained within ~10 minutes

363   (less for isotropic inversions).

364   The PSI inversion methodology has been tested on synthetic models of oceanic plate subduction, intra-oceanic upwelling

365   plume, spreading oceanic ridge, and Central-Eastern Mediterranean subduction (VanderBeek and Faccenda, 2021; Lo Bue et

366   al., 2022, VanderBeek et al., 2023; Faccenda and VanderBeek, 2023), and applied to the isotropic and anisotropic imaging of

367   the Central Mediterranean (Rappisi et al., 2022) and of the Mt. Etna volcanic field (Lo Bue et al., 2023). In Figure 9, we

368   illustrate results obtained from a synthetic inversion of direct teleseismic P- and S-wave relative travel-times computed through

369   the subduction zone shown in Figure 5. Synthetic data were computed using the full 21-component elastic tensor while the

370   inversion was performed for the best-fit hexagonal anisotropic parameters. We considered an array of 770 receivers extending

371   from ±7.5° in longitude and ±11.5° in latitude (~75 km spacing) that recorded 16 events; 8 at a range 50° and another 8 at 80°

372   from the origin of the subduction zone model and equally distributed in back-azimuth. This example is included in the PSI

373   package.

374
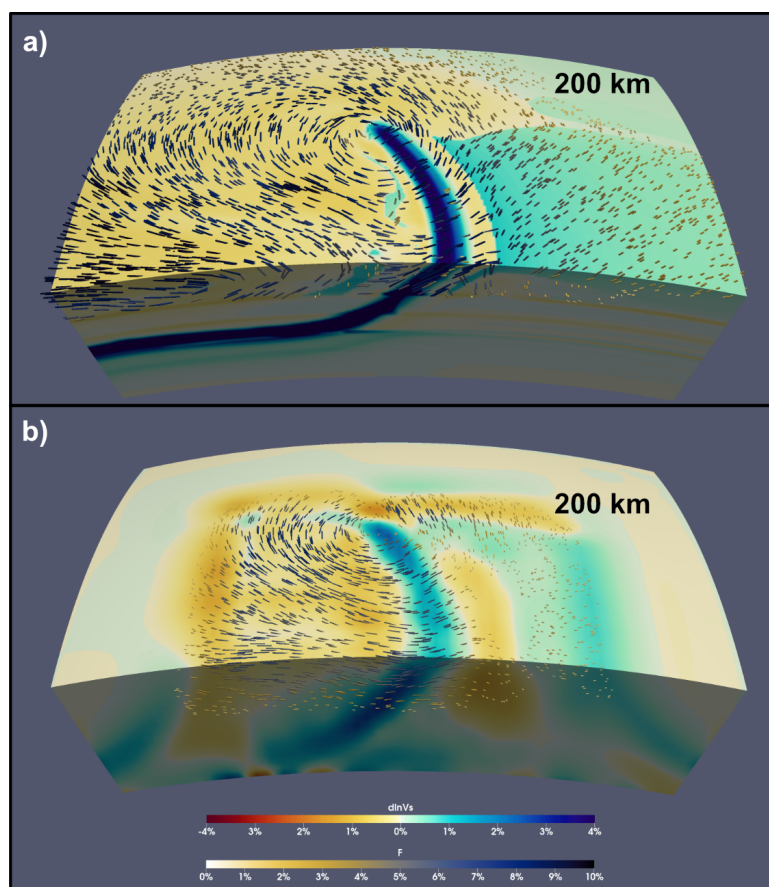
Figure 9. Synthetic tomography results obtained from PSI. (a) Target anisotropic model generated from VIZTOMO. (b) Recovered
anisotropic model obtained by inverting synthetic teleseismic P and S (relative) delay times computed from the model in (a). In both panels,
the isotropic S-wave velocity perturbations are computed with respect to the far-field 1D velocity profile. Quivers parallel the hexagonal

378 symmetry axis and are scaled and coloured by the anisotropic strength. The top surface shown is located at 200 km depth while the full
379 model extends from 0-1000 km along the radial direction, 85°-115° along longitude, and 0-20° along latitude.

3 Discussion

3.1 Software advantages

When compared to other similar software, ECOMAN (i) aims at being a more versatile package suitable for any geodynamic simulations (2D and 3D; cartesian and polar coordinate systems; regional and global settings), (ii) takes into account the time-dependent deformational history of the mantle (which is usually not steady-state, especially close to plate boundaries), (iii) predicts the strain-induced fabric and elastic tensor of different mantle layers (i.e., not only the upper mantle), (iv) includes Effective Medium Theories (STILWE, DEM) and a parametrization of the fabric evolution of two-phase composites to predict elastic and viscous extrinsic anisotropy, (v) generates realistic grid structure distributions of mantle elastic properties to be used for forward/inverse seismological modelling (e.g., PSI, SPECFEM3D), and (vi) performs synthetic seismic inversions (e.g., P- and S-wave travel-time tomographies, S-wave splitting intensities) within the computational domain, which facilitates the comparison with other tomographic models and the estimation of apparent anomalies (artefacts) due to, for example, unaccounted-for elastic anisotropy (Bezada et al., 2016; VanderBeek and Faccenda, 2021; VanderBeek et al., 2023) and/or regularisation.

3.2 Software (real or potential) limitations

D-REX_S and D-REX_M compute the strain-induced LPO for the most abundant and highly anisotropic mineral phases, while assuming random orientation for several secondary phases that instead could contribute substantially to the aggregate anisotropic properties. For example, cubic ferropericlase is relatively abundant (< 20%) and becomes highly anisotropic in the lower half of the lower mantle (Avs = 30-50%), such that it could dominate seismic anisotropy at these depths (Marquardt et al., 2009). Davemaoite (Ca-perovskite) is also a highly anisotropic mineral with cubic symmetry (AVs = 25-15%, Kawai and Tsuchiya, 2015) but its model abundance is quite low (< 10%). Recently, micromechanical simulations of strain-induced LPO in aggregates with a pyrolite mantle composition have shown that the bulk aggregate seismic anisotropy is controlled by bridgmanite and post-perovskite, while the cubic secondary phases appear to only slightly reduce the amplitude of anisotropy (Chendler et al., 2021). The latter effect can thus be well approximated by randomising the orientation of the cubic phases as assumed here.

A main limitation of ECOMAN is that it does not include yet the modelling of viscous anisotropy due to the intrinsic mechanical anisotropy of crystals. Tommasi et al. (2009), have used VPSC simulations to show that olivine CPO in the lithosphere can control the reactivation of fossil faults misoriented with respect to the stress field. Kiraly et al (2020), employed the modified director method (MDM) and estimated up to 1 order of magnitude of intrinsic viscous anisotropy in olivine aggregates, which can control the kinematics and dynamics of tectonic plates. Both the VPSC and MDM approaches are

409 computationally expensive and appear to be prohibitive for the number of mantle aggregates required to discretize the mantle

410 domain of large-scale 3D simulations. An alternative approach which minimises the computational time is therefore desired.

411 A minor limitation is that the different code modules are based on different programming languages (Fortran, Julia), libraries

412 (OpenMP, MPI, HDF5) and software (MATLAB, ParaView), whose installation on local devices might discourage potential

413 users. There are a few main reasons for this. First of all, the original D-REX software was written in Fortran, thus its

414 modifications into D-REX_S and D-REX_M software was more straightforward by maintaining the same programming

415 language. Fortran has high performance standards on HPC clusters, often if not always higher than other high-level

416 programming languages (e.g., MATLAB or Python). Given the large-scale computational power needed for the D-REX_M

417 simulations, especially those with 100.000s or millions of crystal aggregates, and considering that the required compilers and

418 libraries are routinely installed in most (if not all) HPC clusters, the usage of the ECOMAN's Fortran-based applications in

419 high-performance environments is warranted. In contrast, the visualisation of the Fortran-based applications' output in

420 MATLAB and ParaView can be performed on local devices. In particular, the MTEX software is a MATLAB toolbox for

421 visualisation of the LPO and elastic tensor pole figures which should be downloaded ([https://mtex-](https://mtex-toolbox.github.io/download)

422 [toolbox.github.io/download](https://mtex-toolbox.github.io/download)) and installed along with MATLAB only when using D_REX_S. Seismic forward/inverse

423 modelling with PSI can be performed on either a HPC cluster or local devices upon installation of the Julia package. Julia was

424 chosen because it's an open-source and high-level language that offers a number of performance benefits over other popular

425 scientific computing languages such as Python or Matlab. It is important to stress that for any of these applications the user

426 only needs to modify input text files, and thus no particular prerequisite or computational skill is required.

427 Finally, running D-REX_M requires allocating ~ 160 GB of memory per million of crystal aggregates with 1000 x 2 crystals

428 each. This potential problem can be addressed by distributing the computational and memory load over several CPUs, which

429 is possible thanks to the hybrid MPI and OpenMP parallelization scheme.

4 Conclusions and outlook

431 ECOMAN is an open-source software package for estimating strain/stress-induced fabrics in mantle aggregates, their

432 mechanical properties, and how mechanical anisotropy affects the geodynamic evolution and seismic imaging of the Earth's

433 interior. Programs included in ECOMAN are portable across different HPC and local device systems (provided the Julia

434 package and Fortran compilers are available), and are applicable to any 2D-3D geodynamic simulation. Computationally

435 expensive programs such as D-REX_M are parallelized, offering a nearly perfect scaling with an increasing number of cores.

436 As a result, the strain-induced fabrics of millions of mantle aggregates can now be estimated with a reasonable amount of time

437 and computational resources.

438 As ongoing developments, we are seeking to include in ECOMAN micromechanical modelling

439 methods that are capable of estimating the strain−induced LPO and/or the intrinsic viscous

440 anisotropy at computational speeds that are orders of magnitude faster than current ones.

441 `For instance, Ribe et al. (2019), have proposed an analytical finite−strain parameterization`

442 `for texture evolution in deforming olivine polycrystals that is` $\approx 10^7$ times faster than full

443 homogenization approaches such as the second-order self-consistent model. When implemented in ECOMAN, preliminary

444 tests indicate that this new method outperforms D-REX by 1-2 orders of magnitude (Ribe et al., 2023).

445 In addition, in the near future the PSI software will be updated to include trans-dimensional Bayesian Monte Carlo sampling

446 methods that, in contrast to deterministic approaches, address the consequences of under-determination in seismic imaging

447 (Del Piccolo et al., 2023). Isotropic and anisotropic seismic imaging with PSI is currently feasible using body wave information

448 such as travel-times and S-wave splitting intensity. However, when local deep seismicity is absent, as is the case in warm

449 subduction zones or at spreading ridges and intraplate settings, the retrieved isotropic and anisotropic mantle structures are

450 only partially recovered and often affected by smearing (e.g., Faccenda and VanderBeek, 2023). Consequently, we are

451 planning to complement body wave information with surface waves data to improve the seismic ray coverage and the resolving

452 power of tomographic models. Lastly, to improve the prediction of seismic observables, 3D anisotropic ray tracing and finite-

453 frequency kernels are planned for a future release.

454 **Code availability**

455 ECOMAN is freely available at https://github.com/ecoman-geos.

456 **Data availability**

457 The software package contains the input files to generate the synthetic models and datasets discussed in this manuscript. No

458 data has been produced for this work.

459 **Author contributions**

460 MF and BPV developed the software package, with important contributions from AdM and JY. MF wrote the manuscript draft.

461 MF acquired the funding supporting the research activities. All authors have contributed to the discussion and manuscript

462 editing.

463 **Competing interests**

464 The authors declare that they have no conflict of interest.

References

Ahrens, J., Geveci, B., and Law, C.: ParaView: An End-User Tool for Large Data Visualization, in: Visualization Handbook, edited by: Hansen, C.D. and Johnson, C.R., Elsevier, 717-731, https://doi.org/10.1016/B978-012387582-2/50038-1, 2005.

Almqvist, B.S.G. and Mainprice, D. Seismic properties and anisotropy of the continental crust: Predictions based on mineral texture and rock microstructure. Rev. Geophys., 55, 367–433, https://doi.org/10.1002/2016RG000552, 2017.

Becker, T.W., Chevrot, S., Schulte-Pelkum, V. and Blackman, D.K.: Statistical properties of seismic anisotropy predicted by upper mantle geodynamic models. J. Geophys. Res., 111, B08309 https://doi.org/10.1029/2005JB004095, 2006.

Bezada, M., Faccenda, M. and Toomey, D. R: Representing anisotropic subduction zones with isotropic velocity models: A characterization of the problem and some steps on a possible path forward. Geochem. Geophys. Geosyst., https:/doi.org/10.1002/2016GC006507, 2016.

Browaeys, J.T. and Chevrot, S.: Decomposition of the elastic tensor and geophysical applications. Geophys. J. Int., 159, 2, 667–678, 2004.

Bunge, H.-P., Hagelberg, C.R. and Travis, B.J.: Mantle circulation models with variational data assimilation: inferring past mantle flow and structure from plate motion histories and seismic tomography. Geophys. J. Int., 152, 280–301, 2003.

Chandler, B.C., Chen, L.-W., Li, M., Romanowicz, B. and Wenk, H.-R.: Seismic anisotropy, dominant slip systems and phase transitions in the lowermost mantle. Geophys. J. Int., 227, 1665-1681, https://doi.org/10.1093/gji/ggab278, 2021.

Chang, S.-J., Ferreira, A. M. G., Ritsema, J., van Heijst, H. J. and Woodhouse, J. H. Joint inversion for global isotropic and radially anisotropic mantle structure including crustal thickness perturbations. Journal of Geophysical Research: Solid Earth, 120, 4278–4300. https://doi.org/10.1002/2014JB011824., 2015

Chang, S.-J., Ferreira,A.M.G. and Faccenda, M. Upper- and mid-mantle interaction between the Samoan plume and the Tonga-Kermadec slabs. Nat. Commun., 7:10799, https://doi.org/10.1038/ncomms10799, 2016.

494   Chust, T.C., Steinle-Neumann, G., Dolejs, D., Schuberth, B.S. and Bunge, H.P.: MMA- EoS: a computational framework for
495   mineralogical thermodynamics. J. Geophys. Res. 122, 9881–9920, 2017.

496   Crameri, F., and Tackley, P. J. Spontaneous development of arcuate single-sided subduction in global 3-Dmantle convection
497   models with a free surface. J. Geophys. Res. Solid Earth, 119, 921–5942, https://doi:10.1002/2014JB010939 , 2014.

498   Davies, D.R., Goes, S., Davies, J.H., Schuberth, B.S.A., Bunge, H.-P. and Ritsema, J.. Reconciling dynamic and seismic
499   models of Earth's lower mantle: The dominant role of thermal heterogeneity. Earth Planet. Sci. Lett., 353–354, 253-
500   269, 2012.

501   de Montserrat, A., Faccenda, M., and Pennacchioni, G.: Extrinsic anisotropy of two-phase Newtonian aggregates: Fabric
502   characterization and parameterization. J. Geophys. Res.: Solid Earth, 126, e2021JB022232.
503   https://doi.org/10.1029/2021JB022232, 2021.

504   Debayle, E., Bodin, T., Durand, S. and Ricard, Y.. Seismic evidence for partial melt below tectonic plates. Nature 586, 555–
505   559. https://doi.org/10.1038/s41586-020-2809-4, 2020.

506   Del Piccolo, G., VanderBeek, B., Faccenda, M., Morelli, A., and Byrnes, J.: Reversible-Jump, Markov-Chain Monte Carlo
507   seismic tomographic inversion for anisotropic structure in subduction zones (No. EGU23-9927). Copernicus
508   Meetings, https://doi.org10.5194/egusphere-egu23-9927, 2023.

509   Deuss, A. Heterogeneity and anisotropy of Earth's inner core. Annu. Rev. Earth. Planet. Sci. 42, 103–126,
510   https://doi.org/10.1146/annurev-earth-060313-054658, 2014.

511   Faccenda M. and Capitanio, F. A.: Development of mantle seismic anisotropy during subduction-induced 3D flow. Geophys.
512   Res. Lett., 39, https://doi.org/10.1029/2012GL051988, 2012.

513   Faccenda M. and Capitanio, F. A.: Seismic anisotropy around subduction zones: insights from three-dimensional modeling of
514   upper mantle deformation and SKS splitting calculations. Geochem. Geophys. Geosyst.,
515   https://doi.org/10.1002/ggge.20055, 2013.

516   Faccenda, M.: Mid mantle seismic anisotropy around subduction zones, Phys. Earth Planet. Int., 227, 1–19., 2014

517   Faccenda, M., Ferreira, A.M.G., Tisato, N., Lithgow-Bertelloni, C., Stixrude, L. and Pennacchioni, G.: Extrinsic anisotropy in
518   a compositionally heterogeneous mantle. J. Geophys. Res. 124, https://doi.org/10.1029/2018JB016482, 2019.

519   Ferreira, A.M.G., Faccenda, M., Sturgeon, W., Chang, S.-J. and Schardong, L.: Ubiquitous lower-mantle anisotropy beneath
520   subduction zone. Nature Geo. 12, 301-306, https://doi.org/10.1038/s41561-019-0325-7, 2019.

521   Faccenda, M. and VanDerBeek, B.P.: On constraining 3D seismic anisotropy in subduction, mid-ocean-ridge, and plume
522   environments with teleseismic body wave data. J. Geodyn., 158, https://doi.org/10.1016/j.jog.2023.102003, 2023.

523   Fraters, M. R. T. and Billen, M. I.: On the implementation and usability of crystal preferred orientation evolution in
524   geodynamic modeling. Geochem., Geophys., Geosys., 22, e2021GC009846. https://doi.org/10.1029/2021GC009846,
525   2021.

526   French, S., and Romanowicz, B. Broad plumes rooted at the base of the Earth's mantle beneath major hotspots. Nature 525,
527   95–99, https://doi.org/10.1038/nature14876, 2015.

528   Jadamec, M. and Billen, M.: Reconciling surface plate motions with rapid three-dimensional mantle flow around a slab edge.
529   Nature 465, 338–341, https://doi.org/10.1038/nature09053, 2010.

530   Kageyama, A. and Sato, T: ''Yin-Yang grid'': An overset grid in spherical geometry. Geochem Geophys. Geosys., 5, 9,
531   https://doi.org/10.1029/2004GC000734, 2004.

532   Kaminski, E., Ribe, N. M. and Browaeys, J. T.: D-Rex, a program for calculation of seismic anisotropy due to crystal
533   lattice preferred orientation in the convective upper mantle. Geophys. J. Int., 158(2), 744–752.
534   https://doi.org/10.1111/j.1365-246x.2004.02308.x, 2004.

535   Karato, S.-I.: Seismic anisotropy in the deep mantle, boundary layers and the geometry of mantle convection. Pure and Applied
536   Geophysics, 151(2-4), 565–587. https://doi.org/10.1007/s000240050130, 1998.

537   Kawai, K. and Tsuchiya, T.: Small shear modulus of cubic CaSiO3 perovskite. Geophys. Res. Lett., 42, 8,
538   https://doi.org/10.1002/2015GL063446, 2015.

539   Kendall, J.-M.:. Seismic anisotropy in the boundary layers of the mantle. In Earth's deep interior: Mineral physics and
540   tomography from the atomic to the global scale, Geophysical Monograph Series, 117, 133–159, Washington, DC:
541   American Geophysical Union, 2000.

542   Kim, E., Kim, Y. and Mainprice, D.: AnisEulerSC: A MATLAB program combined with MTEX for modeling the anisotropic
543   seismic properties of a polycrystalline aggregate with microcracks using self-consistent approximation. Comp. &
544   Geosci., 145, 104589, https://doi.org/10.1016/j.cageo.2020.104589, 2020.

545   Király, Á., Conrad, C. P. and Hansen, L. N.: Evolving viscous anisotropy in the upper mantle and its geodynamic implications.
546   Geochem. Geophys., Geosys., 21, e2020GC009159, https://doi.org/10.1029/2020GC009159, 2020.

547   Kocher, T. Schmalholz, S.M. and Mancktelow, N.S. Impact of mechanical anisotropy and power-law rheology on single layer
548   folding. Tectonophys. 421, 1-2, 71-87, 2006.

549   Komatitsch, D. and Tromp, J.: Introduction to the spectral element method for three-dimensional seismic wave propagation,
550   Geophys. J. Int., 139(3), 806–822, 1999.

551   Hedjazian, N., Garel, F., Rhodri Davies, D. and Kaminski: E. Age-independent seismic anisotropy under oceanic plates
552   explained by strain history in the asthenosphere. Earth Planet. Sci. Lett. 460, 135-142, 2017.

553   Hu, J., Faccenda, M. and Liu, L.. Subduction-controlled mantle flow and seismic anisotropy in South America. Earth and
554   Planet. Sci. Lett. 470, 13-24, https://doi.org/10.1016/j.epsl.2017.04.027, 2017

555   Li, Z.-H., Di Leo, J.F. and Ribe, N. M. Subduction-induced man-tle flow, finite strain, and seismic anisotropy: Numerical
556   modeling, J. Geophys. Res. Solid Earth,119, 5052–5076, https://doi:10.1002/2014JB010996, 2014.

557   Lo Bue, R., Faccenda, M. and Yang, J.: The role of Adria Plate Lithospheric Structures on the Recent Dynamics of the Central
558   Mediterranean Region. J. Geophys. Res., 126, e2021JB022377. https://doi.org/10.1029/2021JB022377, 2021.

559   Lo Bue, R., Rappisi, F., VanderBeek, B.P. and Faccenda, M.: Tomographic Image Interpretation and Central-Western
560   Mediterranean-Like Upper Mantle Dynamics From Coupled Seismological and Geodynamic Modeling Approach.
561   Front. Earth Sci., 10:884100, https://doi.org/10.3389/feart.2022.884100, 2022.

562   Lo Bue, R., Faccenda, M., Cocina, O., Rappisi, F. and Vanderbeek, B.P.: Joint Active and Passive P-wave
563   Tomography reveals Mt. Etna's Seismic Anisotropy (No EGU23-8563). Copernicus Meetings,
564   https://doi.org/10.5194/egusphere-egu23-8563, 2023.

565   Long, M.D. and Becker, T.W.: Mantle dynamics and seismic anisotropy. Earth Planet. Sci. Lett., 297, 341-354, 2010.

566   Maguire, R., Ritsema, J., Bonnin, M., van Keken, P. E. and Goes, S.: Evaluating the resolution of deep mantle plumes in
567   teleseismic traveltime tomography. J. Geophys. Res., 123, 384–400. https://doi.org/10.1002/2017JB014730, 2018.

568   Mainprice, D.: Modelling the anisotropic seismic properties of partially molten rocks found at mid-ocean ridges. Tectonophys.,
569   279, 1-4, 161-179, 1997.

570   Mainprice, D., Hielscher, R. and Schaeben, H.: in Prior, D.J., Rutter, E.H., Tatham, D. J. Calculating anisotropic physical
571   properties from texture data using the MTEX open source package. (eds) Deformation Mechanisms, Rheology and
572   Tectonics: Microstructures, Mechanics and Anisotropy. Geological Society, London, Special Publications, 360, 175-
573   192, 2011.

574   Marquardt, H., Speziale, S., Reichmann, H. J., Frost, D. J., Schilling, F. R. and Garnero, E.J.: Elastic Shear Anisotropy of
575   Ferropericlase in Earth's Lower Mantle. Science, 324, 5924, 224-226, https://doi.org/10.1126/science.1169365, 2009

576   Müller, R. D., Flament, N., Cannon, J., Tetley, M. G., Williams, S. E., Cao, X., Bodur, Ö. F., Zahirovic, S., and Merdith, A.:
577   A tectonic-rules-based mantle reference frame since 1 billion years ago – implications for supercontinent cycles and
578   plate–mantle system evolution, Solid Earth, 13, 1127–1159, https://doi.org/10.5194/se-13-1127-2022, 2022.

579   Oganov, A.R. and Ono, S.: Theoretical and experimental evidence for a post-perovskite phase of MgSiO3 in Earth's D″ layer.
580   Nature, 430, 445–448, 2004.

581   Rappisi, F., VanderBeek, B., Faccenda, M., Morelli, A. and Molinari, I: Slab geometry and upper mantle flow patterns in the
582   Central Mediterranean from 3D anisotropic P-wave tomography. J. Geophys. Res. 127, e2021JB023488,
583   https://doi.org/10.1029/2021JB023488, 2022.

584   Ribe, N.M., Hielscher, R.H. and Castelnau, O.: An analytical finite-strain parameterization for texture evolution in deforming
585   olivine polycrystals. Geophys. J. Int., 216, 486–514, https://doi.org/10.1093/gji/ggy442, 2019.

586   Ribe, N.M., Faccenda, M., Hielscher, R.H.: SBFTEX: An Analytical Parameterization for Finite Strain-Induced Upper-Mantle
587   Anisotropy. AGU Fall Meeting 2023, DI42A-08, 2023.

588   Rudolph, M.L., Lekić, V. and Lithgow-Bertelloni, C.: Viscosity jump in Earth's mid-mantle. Science, 350, 1349-
589   1352, https://doi.org/10.1126/science.aad1929 , 2015.

590   Schaeffer, A.J., Lebedev, S. and Becker, T.W. Azimuthal seismic anisotropy in the Earth's upper mantle and the thickness of
591   tectonic plates. Geophys. J.l Int., 207, 2, 901–933, https://doi.org/10.1093/gji/ggw309, 2016.

592   Schuberth, B.S.A., Zaroli, C. and Nolet, G.: Synthetic seismograms for a synthetic Earth: long-period P- and S-wave traveltime
593   variations can be explained by temperature alone, Geophys. J. Int., 188(3), 1393–1412, doi:10.1111/j.1365-
594   246X.2011.05333.x, 2012.

595   Schulte-Pelkum, V. and Blackman, D.K.: A synthesis of seismic P and S anisotropy, J. Geophys. Int., 154, 1, 166–178, 2003.

596   Shea Jr, W. T. and Kronenberg, A. K. Strength and anisotropy of foliated rocks with varied mica contents. Journal of Structural
597   Geology, 15(9-10), 1097-1121, https://doi.org/10.1016/0191-8141(93)90158-7, 1993.

598   Steinberger, B. and Calderwood, A.: Models of large-scale viscous flow in the Earth's mantle with constraints from mineral
599   physics and surface observations. Geophys. J. Int., 167, 1461-1481, https://doi.org/10.1111/j.1365-
600   246X.2006.03131.x, 2006

601   Styles, E., Davies, D. R., and Goes, S.:. Mapping spherical seismic into physical structure: Biases from 3-D phase-transition
602   and thermal boundary-layer heterogeneity. Geophys. J. Int., 184, 1371–1378. https://doi.org/10.1111/j.1365-
603   246X.2010.04914.x , 2011.

604   Sturgeon W., Ferreira, A.M.G., Faccenda, M., Chang, S.-J. and Schardong, L.: On the origin of radial anisotropy near
605   subducted   slabs   in   the   midmantle.   Geochem.   Geophys.   Geosys.   20   (11),   5105-5125,
606   https://doi.org/10.1029/2019GC008462, 2019.

607   Tommasi, A., Knoll, M., Vauchez, A., Signorelli, J. W., Thoraval, C. and Logé, R.: Structural reactivation in plate tectonics
608   controlled by olivine crystal anisotropy. Nature Geosci., 2, 423–427, https://doi.org/10.1038/ngeo528, 2009.

609   VanderBeek, B.P., Faccenda, M.: Imaging upper mantle anisotropy with teleseismic P-wave delays: insights from tomographic
610   reconstructions of subduction simulations. Geophys. J. Int. 225, 2097–2119, 2021.

611   VanderBeek, B.P., Lo Bue, R., Rappisi, F. and Faccenda, M.: Imaging upper mantle anisotropy with travel-time and splitting
612   intensity observations from teleseismic shear waves: Insights from tomographic reconstructions of subduction
613   simulations. https://doi.org/10.1093/gji/ggad389, 2023.

614   Halter, W., Macherel, E., Duretz, T., and Schmalholz, S. M. Numerical modelling of strain localization by anisotropy evolution
615   during 2D viscous simple shearing, EGU General Assembly 2022, Vienna, Austria, 23–27 May 2022, EGU22-11438,
616   https://doi.org/10.5194/egusphere-egu22-11438, 2022.

617   Zhou, Q., Hu, J., Liu, L., Chaparro, T., Stegman, D. R. and Faccenda, M.: Western U.S. seismic anisotropy revealing complex
618   mantle dynamics. Earth and Planet. Sci. Lett. 500, 156-167, https://doi.org/10.1016/j.epsl.2018.08.015, 2018.